Earth Planets Space, **61**, 835–843, 2009

Application of GOCE data for regional gravity field modeling

Juraj Janák[1], Yoichi Fukuda[2], and Peiliang Xu[3]

[1]*Department of Theoretical Geodesy, Slovak University of Technology, Radlinského 11, 81368 Bratislava, Slovakia*
[2]*Department of Geophysics, Kyoto University, Sakyo-ku, Kyoto 606-8502, Japan*
[3]*Disaster Prevention Research Institute, Kyoto University, Uji, Kyoto 611-0011, Japan*

(Received July 25, 2008; Revised March 12, 2009; Accepted March 16, 2009; Online published August 31, 2009)

In principle, every component of a disturbing gravity gradient tensor measured in a satellite orbit can be used to obtain gravity anomalies on the Earth's surface. Consequently, these can be used in combination with ground or marine data for further gravity field modeling or for verification of satellite data. Theoretical relations can be derived both in spectral and spatial forms. In this paper, we focus on the derivation of a spatial integral form in the geocentric spherical coordinates that seems to be the most convenient one for regional gravity field modeling. All of the second partial derivatives of the generalized Stokes's kernel are derived, and six surface Fredholm integral equations are formulated and discretized. The inverse problems formulated for particular components clearly reveal different behaviors in terms of numerical stability of the solution. Simulated GOCE data disturbed with Gaussian noise are used to study the performance of two regularization methods: truncated singular value decomposition and ridge regression. The optimal ridge regression method shows slightly better results in terms of the root mean squared deviation of the differences from the exact solution.
Key words: Gradiometry, Pizzetti integral formula, inverse problem, regularization.

1. Introduction

The entire geo-scientific community is restlessly awaiting the launch of the GOCE (Gravity Field and Steady-State Ocean Circulation Explorer) satellite mission. This satellite will globally cover the whole Earth, except for small polar gaps, with highly accurate measurements of the second derivatives of the Earth gravitational potential. These measurements will be taken at an approximate altitude of 250–260 km, depending on the orbit scenario selected (see, for example, Drinkwater *et al*., 2007 for details).

In order to use the GOCE SGG (Satellite Gravity Gradiometry) data for regional gravity field modeling, such as for precise geoid computation, it would be useful to continue these data downward to the surface of the Earth or to a geoid. Moreover, if the downward continuation is successful and accurate enough, it will be possible to use it for external validation of the GOCE data with accurate ground data. The approach derived and proposed in this paper is able to use all six different components of the disturbing gravity gradient tensor at the flight level by converting them into a free-air gravity anomaly at different levels outside the real or regularized Earth. However, we do realize that several important practical obstacles are not treated here, as they are beyond the scope of this paper: (1) only four of the six components of the gravity gradient tensor will be measured with a high degree of accuracy, while the other two components will be degraded (European Space Agency, 2006); (2) the data will be measured along an orbit track and not on a regular grid; (3) the data will be measured in a gradiometer reference frame, which deviates from an ideal horizontal reference frame; (4) the noise of the data will be coloured, leading to strong along-track correlations. Nevertheless, we believe the results published in this paper show the possible general performance obtainable with the real GOCE data.

The paper is organized as follows. First, the theoretical background and mathematical derivation are given; this is followed by an investigation of the properties of the derived integration kernels and, finally, by the numerical simulation. The last section focuses primarily on the quality of the solution as in Xu (1992, 1998), since we have to deal here with the inverse problem of downward continuation.

2. Theoretical Background

Let us begin with the Pizzetti integral formula (Pizzetti, 1911; Heiskanen and Moritz, 1967)

$$T(r, \Omega) = \frac{R}{4\pi} \int_{\Omega'} \Delta g(\Omega') S(r, \psi, R)\, d\Omega', \qquad (1)$$

where T is the disturbing gravity potential, Δg is the free-air gravity anomaly (the magnitude of the gravity anomaly vector), and S stands for the generalized Stokes's function given by

$$S(r, \psi, R) = \frac{2R}{\ell} + \frac{R}{r} - \frac{3R\ell}{r^2} - \frac{R^2}{r^2}\cos\psi \cdot \left(5 + 3\ln\frac{r - R\cos\psi + \ell}{2r}\right). \qquad (2)$$

We use a geocentric spherical coordinate system, where Ω represents the horizontal position, given by a pair of the geocentric angular coordinates of the latitude and longitude

(φ, λ), and the vertical position is given by the geocentric radial distance r. As usual, R is the radius of the reference sphere, ℓ is the spatial Euclidean distance, and ψ is the angular spherical distance between the point of computation and the particular integration element at the horizontal position Ω', i.e. (φ', λ'), see Appendix A for details.

Let us rewrite Eq. (2) using the substitutions

$$t = \frac{R}{r}, \tag{3}$$

$$D = \frac{\ell}{r} = \left(1 + t^2 - 2t\cos\psi\right)^{1/2}, \tag{4}$$

in a numerically stable form (see, for example, Xu, 1992)

$$S(t, \psi) = t\left[\frac{2}{D} + 1 - 3D - t\cos\psi\left(5 + 3\ln\frac{1 - t\cos\psi + D}{2}\right)\right]. \tag{5}$$

We will follow a concept based on using the derivatives of the Pizzetti formula (Eq. (1)) to obtain the relation between the components of the disturbing gravity gradient tensor in a mass-free space expressed in spherical coordinates (Novák and Grafarend, 2006)

$$\mathbf{T}(r, \varphi, \lambda) = \mathrm{grad}\cdot(\mathrm{grad}T) = \nabla\otimes\nabla T(r, \varphi, \lambda) = \begin{pmatrix} T_{\varphi\varphi} & T_{\varphi\lambda} & T_{\varphi r} \\ T_{\lambda\varphi} & T_{\lambda\lambda} & T_{\lambda r} \\ T_{r\varphi} & T_{r\lambda} & T_{rr} \end{pmatrix} \tag{6}$$

and the free-air gravity anomaly on the reference sphere (e.g. Reed, 1973). The symbol ∇ stands for the operator gradient in the spherical coordinates defined as follows (Bronshtein *et al.*, 2004),

$$\nabla = \left(\frac{\partial}{\partial r}, \frac{\partial}{r\,\partial\varphi}, \frac{\partial}{r\cos\varphi\,\partial\lambda}\right)^T. \tag{7}$$

For this purpose we have to express the second derivatives of $S(t(r, R), \psi(\varphi, \lambda, \varphi', \lambda'))$ according to the variables (r, φ, λ). As the disturbing gravity gradient tensor is symmetrical, there are only six different components, of which only five are linearly independent in a mass-free space. Let us note that Kern and Haagmans (2005) derived the closed expressions for the second derivatives of $S(t(r, R), \psi(\varphi, \lambda, \varphi', \lambda'))$ according to the variables r and ψ. A valuable contribution to the solution of gradiometric boundary-value problems has also been given by van Gelderen and Rummel (2001, 2002) and Martinec (2003).

3. Mathematical Derivation

Let us introduce the following notation:

$$C = \frac{\partial\cos\psi}{\partial\varphi}, \tag{8}$$

$$E = \frac{\partial\cos\psi}{\partial\lambda}, \tag{9}$$

$$F = \frac{\partial^2\cos\psi}{\partial\lambda^2}, \tag{10}$$

$$G = \frac{\partial^2\cos\psi}{\partial\varphi\partial\lambda} = \frac{\partial^2\cos\psi}{\partial\lambda\partial\varphi}. \tag{11}$$

The full formulae for symbols C, E, F, and G, described as functions of the geocentric latitude φ, angular distance ψ, and spherical azimuth of integration element α are shown in Appendix A.

Now, the second derivatives of function $S(t(r, R), \psi(\varphi, \lambda, \varphi', \lambda'))$ according to the variables (r, φ, λ) have been performed, resulting in a tensor-valued kernel function defined as

$$\mathbf{S}(r, \psi, R) = \mathrm{grad}\cdot(\mathrm{grad}S) = \nabla\otimes\nabla S(r, \psi, R) = \begin{pmatrix} S_{\varphi\varphi} & S_{\varphi\lambda} & S_{\varphi r} \\ S_{\lambda\varphi} & S_{\lambda\lambda} & S_{\lambda r} \\ S_{r\varphi} & S_{r\lambda} & S_{rr} \end{pmatrix}. \tag{12}$$

The particular entries of $\mathbf{S}$ are given in Appendix A. The units of these entries are meter^{-2}. Assuming Eqs. (1) and (6), we obtain the tensor-valued equation

$$\mathbf{T}(r, \Omega) = \frac{R}{4\pi}\iint_{\Omega'}\Delta g(R, \Omega')\,\mathbf{S}(r, \psi, R)\,d\Omega'. \tag{13}$$

As we can see from the particular entries of $\mathbf{S}$ in Appendix A, only the second radial derivative of the function S remains homogenous and isotropic; the other second derivatives are no longer isotropic but azimuth-dependent. Moreover, the derivatives according to λ are latitude dependent, i.e., not homogenous. In the case when $\psi = 0$, the azimuth dependency vanishes, $C = E = G = 0$ and $F = -\cos^2\varphi$.

4. Properties of the Derived Integration Kernels

For the purpose of visualization, it is useful to introduce the normalized dimensionless integration kernels as $\tilde{\mathbf{S}} = r^2\mathbf{S}$. Although many particular properties can easily be seen from the figures of the six normalized integration kernels (see Fig. 1(a–f)), let us provide a brief description here. All of the kernel figures have been produced using the following parameters: $\varphi = 35.5^\circ$, $\lambda = 136.5^\circ$ (coordinates of the computation point), $R = 6371$ km (radius of the reference sphere), $h = 250$ km (height of the point of computation above the reference sphere), $\varphi' \in (28^\circ, 43^\circ)$, and $\lambda' \in (127^\circ, 146^\circ)$ (variable coordinates of the integration element).

Provided that $r \neq R$, the integration kernels do not possess any singularity. For the mixed second derivatives, the value at $\psi = 0^\circ$ becomes zero, and for the double derivatives according to the same variable, the value at $\psi = 0^\circ$ is the finite real number dependent only on parameter t. The integration kernel $\tilde{S}_{rr}(t, \psi)$ is homogeneous and isotropic, $\tilde{S}_{\varphi\varphi}(t, \psi, \alpha)$ and $\tilde{S}_{\varphi r}(t, \psi, \alpha)$ are homogeneous but not isotropic, and $\tilde{S}_{\varphi\lambda}(t, \psi, \alpha, \varphi)$, $\tilde{S}_{\lambda\lambda}(t, \psi, \alpha, \varphi)$, $\tilde{S}_{\lambda r}(t, \psi, \alpha, \varphi)$ are neither homogeneous nor isotropic. The function $\tilde{S}_{\varphi\lambda}(t, \psi, \alpha, \varphi)$ is always zero for $\alpha = \{0^\circ, 90^\circ, 180^\circ, 270^\circ\}$ and reaches its maximum and minimum for $\alpha = \{45^\circ, 135^\circ, 225^\circ, 315^\circ\}$ at the approximate spherical distance $\psi \approx 1.5^\circ$ (for $h = 250$ km). The function $\tilde{S}_{\varphi r}(t, \psi, \alpha)$ is zero for $\alpha = \{90^\circ, 270^\circ\}$ and has its maximum for $\alpha = 0^\circ$ and minimum for $\alpha = 180^\circ$ at the $\psi \approx 1.2^\circ$. The function $\tilde{S}_{\lambda r}(t, \psi, \alpha, \varphi)$ is zero for $\alpha = \{0^\circ, 180^\circ\}$, decreases to a minimum for $\alpha = 90^\circ$, and increases to a maximum for $\alpha = 270^\circ$ at $\psi \approx 1.2^\circ$.

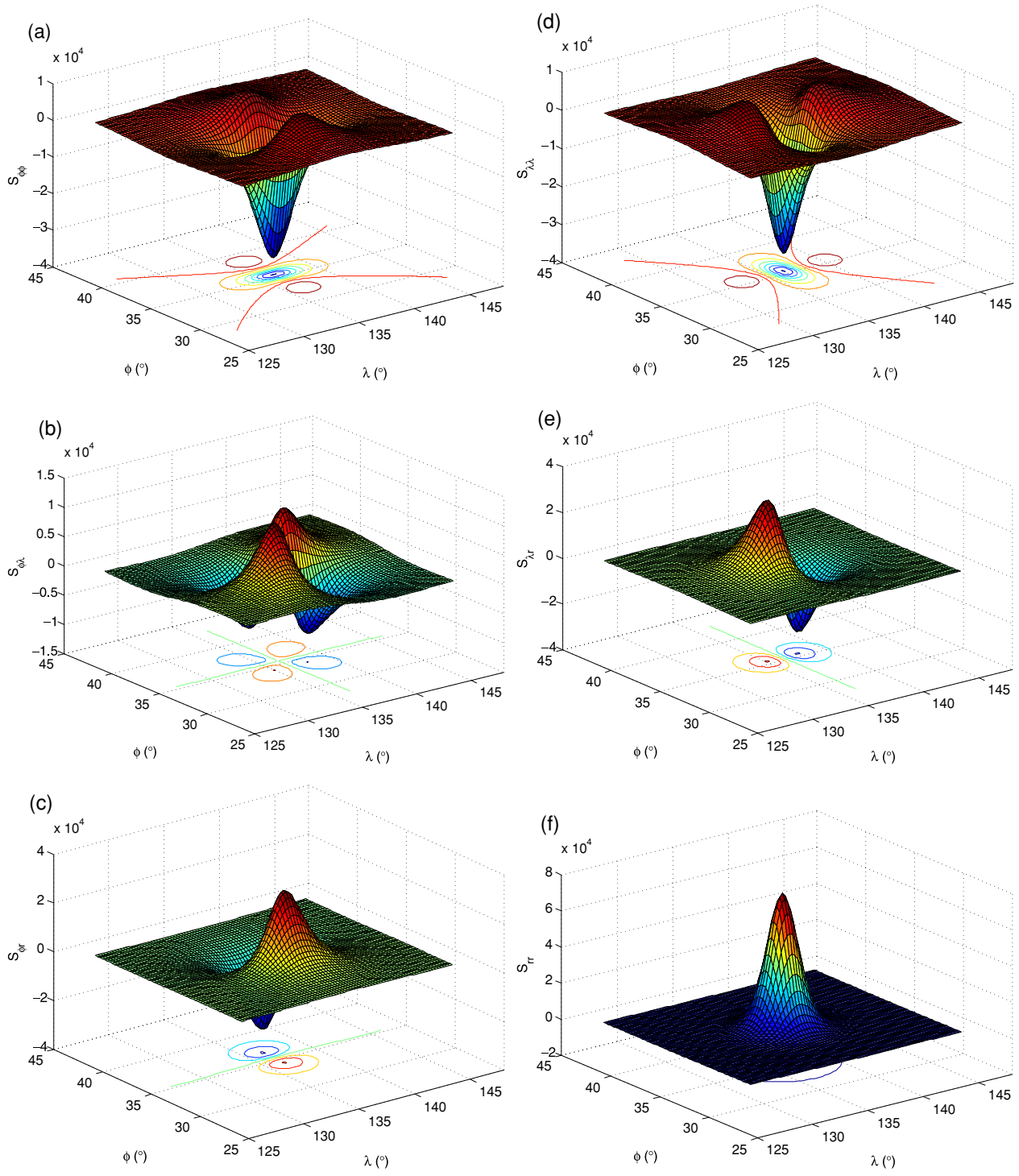

Fig. 1. (a) Normalized integration kernel $\tilde{S}_{\varphi\varphi}(t, \psi, \alpha)$. (b) Normalized integration kernel $\tilde{S}_{\varphi\lambda}(t, \psi, \alpha, \varphi)$. (c) Normalized integration kernel $\tilde{S}_{\varphi r}(t, \psi, \alpha)$. (d) Normalized integration kernel $\tilde{S}_{\lambda\lambda}(t, \psi, \alpha, \varphi)$. (e) Normalized integration kernel $\tilde{S}_{\lambda r}(t, \psi, \alpha, \varphi)$. (f) Normalized integration kernel $\tilde{S}_{rr}(t, \psi)$.

The functions $\tilde{S}_{\varphi\varphi}(t, \psi, \alpha)$ and $\tilde{S}_{\lambda\lambda}(t, \psi, \alpha, \varphi)$ are negative at the vicinity of the computation point and reach zero on the hyperbolic curves. For $\alpha \in (-45^\circ, 45^\circ)$ and $\alpha \in (135^\circ, 225^\circ)$, $\tilde{S}_{\varphi\varphi}(t, \psi, \alpha)$ can also reach positive values (not in the exact vicinity of the computation point), while the maximum values are reached for $\alpha = \{0^\circ, 180^\circ\}$ at $\psi \approx 2.5^\circ$. Conversely, $\tilde{S}_{\lambda\lambda}(t, \psi, \alpha, \varphi)$ can reach positive values for $\alpha \in (45^\circ, 135^\circ)$ and $\alpha \in (225^\circ, 315^\circ)$, with maximum values for $\alpha = \{90^\circ, 270^\circ\}$ at $\psi \approx 2.5^\circ$.

The function $\tilde{S}_{rr}(t, \psi)$ reaches its maximum for the $\psi \approx 0^\circ$ and then simply decreases with the growing spherical distance, reaches zero on a circular curve at the $\psi \approx 3.7^\circ$, then goes down to a small negative minimum at the $\psi \approx 5^\circ$, then slowly approaches zero, and at the $\psi \approx 117^\circ$ again becomes slightly positive.

5. Numerical Simulation

Let us rewrite Eq. (13) into a discrete form, supposing that the gravity anomalies are given as block-mean values

Δg_i (Xu, 1992)

$$\mathbf{T}(r, \Omega) = \frac{R}{4\pi} \sum_{i=1}^{k} \Delta g(\alpha_i, \psi_i)\, \mathbf{S}(t_i, \alpha_i, \psi_i) \Delta s(\alpha_i, \psi_i). \tag{14}$$

Let us note that if the gravity anomalies are given in mGal units (mGal $= 10^{-5}$ m.s^{-2}), radius R in kilometers, and entries of $\mathbf{T}$ in EU (EU = 1 Eötvös unit $= 10^{-9}$ s^{-2}), the left-hand side of Eq. (14) should be divided by a factor of 10.

Suppose we have n observations of every component of the disturbing gravity gradient tensor given in a known horizontal position Ω at the altitude of the satellite orbit and k unknown mean free-air gravity anomalies in a region of interest on the reference sphere and assume $k \leq n$. Let $\boldsymbol{\varepsilon}$ be the error vector of the observations and let $\boldsymbol{\Sigma}$ be the covariance matrix of the observations and $\mathbf{P} = \boldsymbol{\Sigma}^{-1}$ be the weight matrix. We can then create from Eq. (14) six matrix equations, corresponding to particular components of tensor $\mathbf{T}$, in the following form:

$$\mathbf{l} = \mathbf{A}\,\mathbf{x} + \boldsymbol{\varepsilon} \tag{15}$$

As the matrix $\mathbf{A}$ is not necessarily the square matrix and the dimension is (n, k), it is convenient to multiply Eq. (15) by $\mathbf{A}'\mathbf{P}$ from the left, so we can get the least squares (LS) estimate of $\mathbf{x}$

$$\mathbf{A}'\mathbf{P}\,\mathbf{l} = \mathbf{A}'\mathbf{P}\,\mathbf{A}\,\mathbf{x} \Rightarrow \mathbf{b} = \mathbf{B}\,\mathbf{x}. \tag{16}$$

The matrix $\mathbf{B}$ has the dimension of (k, k). Equation (16) represents a system of k linear equations with k unknown parameters, and $\mathbf{B}$ is the matrix of the normal equation coefficients. To solve this system for $\mathbf{x}$, one possibility is to use the LU decomposition of $\mathbf{B}$. Assuming the uniform accuracy of the input data, the LS estimate of $\mathbf{x}$ is obtained from the well-known formula:

$$\hat{\mathbf{x}}_{\mathrm{LS}} = (\mathbf{A}'\mathbf{A})^{-1}\mathbf{A}'\mathbf{l}. \tag{17}$$

As the matrix $\mathbf{B}$ in our inverse problems is ill-conditioned, the input data noise can be extremely magnified in the LS estimate, resulting in a very large standard deviation of the solution. Therefore, some stabilization procedure needs to be applied. We decided to compare two stabilization methods: the quality-based truncated singular value decomposition (TSVD) and the ridge regression (RR) with the optimal ridge parameter.

The TSVD estimate is computed using the following equation (see Xu, 1998)

$$\hat{\mathbf{x}}_{\mathrm{TSVD}} = \sum_{i=1}^{\tau} \frac{\mathbf{u}_i\mathbf{l}}{\lambda_i}\mathbf{v}_i, \tag{18}$$

where λ_i are the eigenvalues of the matrix $\mathbf{B}$ arranged in decreasing order; $\mathbf{u}_i$ and $\mathbf{v}_i$ are the corresponding eigenvectors; $\tau \leq k$ is the integer truncation parameter. For more details on the TSVD method, see, for example, Aster *et al.* (2005) and Xu (1998).

Applying the ridge estimator (Hoerl and Kennard, 1970), the ridge estimate is computed as

$$\hat{\mathbf{x}}_{\mathrm{R}} = (\mathbf{A}'\mathbf{A} + \kappa\mathbf{I})^{-1}\mathbf{A}'\mathbf{l}, \tag{19}$$

where $\kappa > 0$ is the ridge parameter, and $\mathbf{I}$ is the unit matrix of dimension (k, k). For more details about the RR method, see, for example, Xu (1992) and Xu and Rummel (1994).

The key objective in the TSVD and RR methods is to find the optimal truncation parameter τ_{opt} or the optimal ridge parameter κ_{opt}, respectively. Let us assume this is true when dealing with simulated observations; we know the errorless reference output data $\mathbf{x}_{\mathrm{REF}}$. In such a case, we are able to obtain the true error vectors of the estimates (18) and (19)

$$\begin{aligned} \boldsymbol{\varepsilon}_{\mathrm{TSVD}} &= \mathbf{x}_{\mathrm{REF}} - \hat{\mathbf{x}}_{\mathrm{TSVD}}, \\ \boldsymbol{\varepsilon}_{\mathrm{R}} &= \mathbf{x}_{\mathrm{REF}} - \hat{\mathbf{x}}_{\mathrm{R}}, \end{aligned} \tag{20}$$

and, consequently, to compute the corresponding root mean squared errors (RMSE)

$$\begin{aligned} \sigma_{\mathrm{TSVD}} &= \left(\frac{\sum_{i=1}^{k} \varepsilon_{\mathrm{TSVD}i}\, \varepsilon_{\mathrm{TSVD}i}}{k} \right)^{\frac{1}{2}}, \\ \sigma_{\mathrm{R}} &= \left(\frac{\sum_{i=1}^{k} \varepsilon_{\mathrm{R}i}\, \varepsilon_{\mathrm{R}i}}{k} \right)^{\frac{1}{2}}. \end{aligned} \tag{21}$$

The optimal values τ_{opt} and κ_{opt} are those corresponding to the smallest RMSE defined by Eq. (21).

For the numerical simulation of regional gravity field modeling based on satellite gradiometric data, we chose the Far East Asia region with the center in Japan. Our simulation is based on the EGM-96 geopotential model (Lemoine *et al.*, 1998).

The area of the simulated input data is bounded by the parallels $\varphi \in (24^\circ, 46^\circ)$ and the meridians $\lambda \in (126^\circ, 148^\circ)$. The simulated input data are six components of the disturbing gravity gradient tensor in the spherical coordinates generated from the EGM-96 up to the degree and order of 360 at an altitude of 250 km disturbed with the Gaussian noise with a standard deviation of 0.005 EU. The value 0.005 EU has been chosen with respect to the expected GOCE gradiometer noise (see Drinkwater *et al.*, 2007). The simplified assumption of the same degree of accuracy for every component has been considered. The input data are generated in a regular grid $\Delta\varphi \times \Delta\lambda = 0.2^\circ \times 0.2^\circ$, i.e., the number of observations is $n = 110 \times 110 = 12100$. The output data region is the same as the input data region. Let us note that when working with the real measured data in practice, the output region should be smaller in order to avoid the edge effect. In our paper, however, we use the simulated data and do not study the edge effect. The output data are the free-air gravity anomalies on the geoid in a spherical approximation, and no masses above the geoid are assumed. The two different output grid steps have been chosen as follows: (a) $\Delta\varphi \times \Delta\lambda = 2^\circ \times 2^\circ$ for the edge part of the region of interest and $\Delta\varphi \times \Delta\lambda = 1^\circ \times 1^\circ$ for the central part of the region of interest; (b) $\Delta\varphi \times \Delta\lambda = 2^\circ \times 2^\circ$ for the edge part of the region of interest and $\Delta\varphi \times \Delta\lambda = 0.5^\circ \times 0.5^\circ$ for the central part of the region of interest. The central part of the output data region is bounded by the parallels $\varphi \in (30^\circ, 40^\circ)$ and by the meridians $\lambda \in (132^\circ, 142^\circ)$. Using the different output grid step in the edge part of the output data region is convenient from a numerical point of view; mainly, we obtain a smaller

Table 1. RMSE of particular inverse problem solutions for an output data resolution of $1^\circ \times 1^\circ$ (case a). The number of repetitions for every inverse problem is 200. Standard deviation of Gaussian input data noise: 0.005 EU. All values are in mGal units. The best mean RMSE for the particular inverse problem is in bold.

Inv. prob.	for $T_{\varphi\varphi}$	for $T_{\varphi\lambda}$	for $T_{\varphi r}$	for $T_{\lambda\lambda}$	for $T_{\lambda r}$	for T_{rr}	method
σ_{mean}	41.47	15.96	13.11	13.78	7.92	5.66	LS
σ_{min}	16.30	8.13	6.77	7.56	4.09	3.36	
σ_{max}	95.23	27.79	21.62	23.58	15.74	10.51	
σ_{mean}	11.23	8.59	7.31	7.37	5.36	3.98	TSVD
σ_{min}	8.72	6.00	5.19	5.22	3.96	2.86	
σ_{max}	14.40	10.03	9.38	10.00	7.44	5.37	
σ_{mean}	**10.72**	**8.00**	**6.86**	**6.84**	**4.99**	**3.77**	RR
σ_{min}	8.22	5.63	5.18	4.92	3.63	2.49	
σ_{max}	13.79	10.46	8.74	8.60	6.90	5.19	

Table 2. RMSE of particular inverse problem solutions for an output data resolution of $0.5^\circ \times 0.5^\circ$ (case b). The number of repetitions for every inverse problem is 200. Standard deviation of Gaussian input data noise: 0.005 EU. All values are in mGal units. The best mean RMSE for the particular inverse problem is in bold.

Inv. prob.	for $T_{\varphi\varphi}$	for $T_{\varphi\lambda}$	for $T_{\varphi r}$	for $T_{\lambda\lambda}$	for $T_{\lambda r}$	for T_{rr}	method
σ_{mean}	4.34E+05	8.48E+03	1.34E+04	1.05E+05	2.00E+05	1.41E+05	LS
σ_{min}	2.08E+05	6.63E+03	9.15E+03	6.65E+04	8.80E+04	4.47E+04	
σ_{max}	8.16E+05	1.08E+04	1.84E+05	1.49E+05	4.50E+05	3.59E+05	
σ_{mean}	22.25	18.98	17.69	16.56	15.33	14.40	TSVD
σ_{min}	19.83	17.40	16.45	15.55	14.37	13.81	
σ_{max}	23.37	20.58	19.04	17.58	16.20	15.01	
σ_{mean}	**21.00**	**18.37**	**17.01**	**15.95**	**14.78**	**13.84**	RR
σ_{min}	19.03	16.93	15.78	14.75	13.67	13.00	
σ_{max}	22.77	19.78	18.68	16.99	15.83	14.55	

Table 3. Mean percentage of the truncated part of the eigenvalues for the TSVD method and the mean ridge parameter for the RR method computed from 200 repetitions.

Inverse problem	For $T_{\varphi\varphi}$	For $T_{\varphi\lambda}$	For $T_{\varphi r}$	For $T_{\lambda\lambda}$	For $T_{\lambda r}$	For T_{rr}	
χ_{mean} (%)	7.5	6.1	4.3	4.3	2.2	1.5	Case (a)
κ_{mean}	1.14	1.91	2.05	2.41	2.82	3.38	
χ_{mean} (%)	59.8	61.9	58.0	61.0	59.8	56.8	Case (b)
κ_{mean}	0.56	0.86	0.96	1.31	1.76	2.13	

amount of equations and better numerical stability. Eventually, this edge part can be cut off when working with the real data in the future. In case (b), the number of unknowns is $k = 96 + 100 = 196$, and the number of elements in matrix $\mathbf{A}$ is $n \times k = 2371600$. In case (b) $k = 96 + 400 = 496$ and the number of elements in matrix $\mathbf{A}$ is $n \times k = 6001600$.

All six inverse problems (Eq. (14)) have been solved 200 times using the LS, TSVD, and RR methods. For every computation, a new Gaussian noise has been generated and added to the simulated measurements. The advantage of repeated computations is the possibility of obtaining a more reliable comparison when comparing the mean values of RMSE and also the possibility of estimating the second order parameters for every mean RMSE. Moreover, all of the computations have been performed for two different configurations of the output data; see the above cases (a) and (b). The mean RMSE σ_{mean} computed as the average of 200 values obtained from (Eq. (21)) and extreme RMSEs σ_{min}, σ_{max} are given in Table 1 for case (a) and in Table 2 for case (b).

Table 3 shows the average percentage of the truncated eigenvalues χ_{mean}, computed from 200 repetitions, and the mean values of the optimal ridge parameter κ_{mean} for cases (a) and (b). The values χ_{mean} have been computed from the following expression:

$$\chi_{\text{mean}} = \frac{1}{200} \sum_{i=1}^{200} \frac{k - \tau_i}{k}. \tag{22}$$

The condition numbers of the original matrix $\mathbf{B}$ for the par-

Table 4. Condition numbers of normal matrices for particular inverse problems.

Inverse problem	For $T_{\varphi\varphi}$	For $T_{\varphi\lambda}$	For $T_{\varphi r}$	For $T_{\lambda\lambda}$	For $T_{\lambda r}$	For T_{rr}	
Condition	1.1e+08	1.2e+06	4.7e+06	5.8e+06	2.1e+06	1.8e+06	Case (a)
Condition	1.4e+16	1.6e+11	3.2e+12	3.4e+14	4.7e+15	4.1e+15	Case (b)

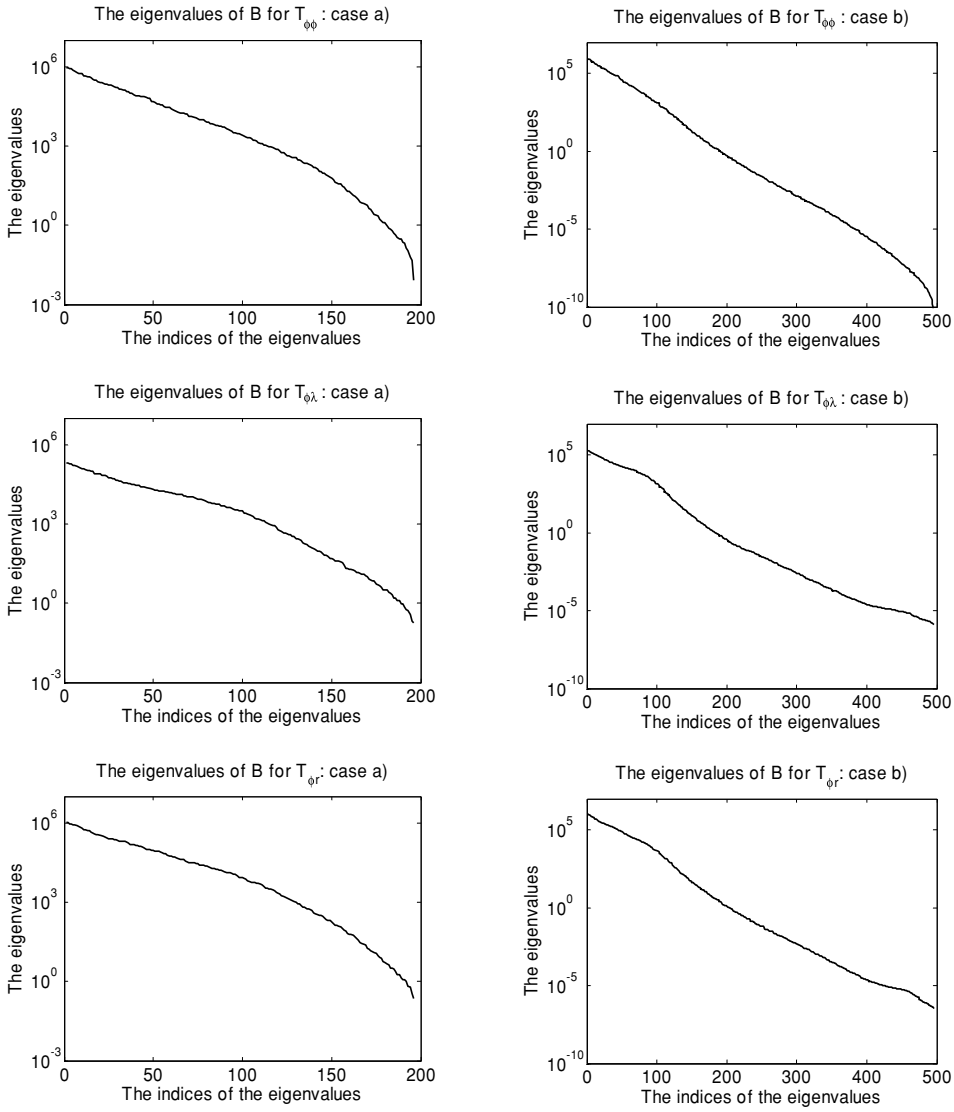

Fig. 2. Graphs of the eigenvalues of the normal equation matrices **B** for the selected inverse problems. The behavior of the other eigenvalues is similar.

ticular inverse problems, computed as the ratio of the largest and smallest eigenvalues, are shown in Table 4. The graphs of the eigenvalues of matrices **B** sorted in decreasing order for the selected inverse problems are shown in Fig. 2. The selected results in terms of the grids of the gravity anomaly differences between the processing results and the true reference are shown in Figs. 3(a) and (b). In analyzing these figures and similar figures corresponding to other components of tensor **T** (not shown in this paper), we can observe a number of features. In case (a), the gravity anomaly differences corresponding to the $T_{\varphi\varphi}$ component reveal the visible systematic north-south stripping, especially in the LS estimate. Also in case (a), the systematic east-west stripping can be found in the differences corresponding to the $T_{\lambda\lambda}$ component. In case (b), this stripping is not so apparent, probably because the random error magnified by the larger numerical instability overlays the systematic effect. No correlation can be seen when the differences with the input signal itself are compared.

Looking at Tables 1–4, we can see that the stability of the solutions in case (b) is much worse than that in case (a). This phenomenon was expected, and it is related to the discretization step, i.e., the smaller the step, the higher the degree of instability. From this point of view, the discretization on its own also represents the regularization of the solution. In case (b), the instability of the solutions is so high that the LS estimate is useless. It is interesting to note that the RR estimate provides slightly better results on average than the TSVD estimate for all the particular solutions.

In Table 4, we can compare the condition numbers for

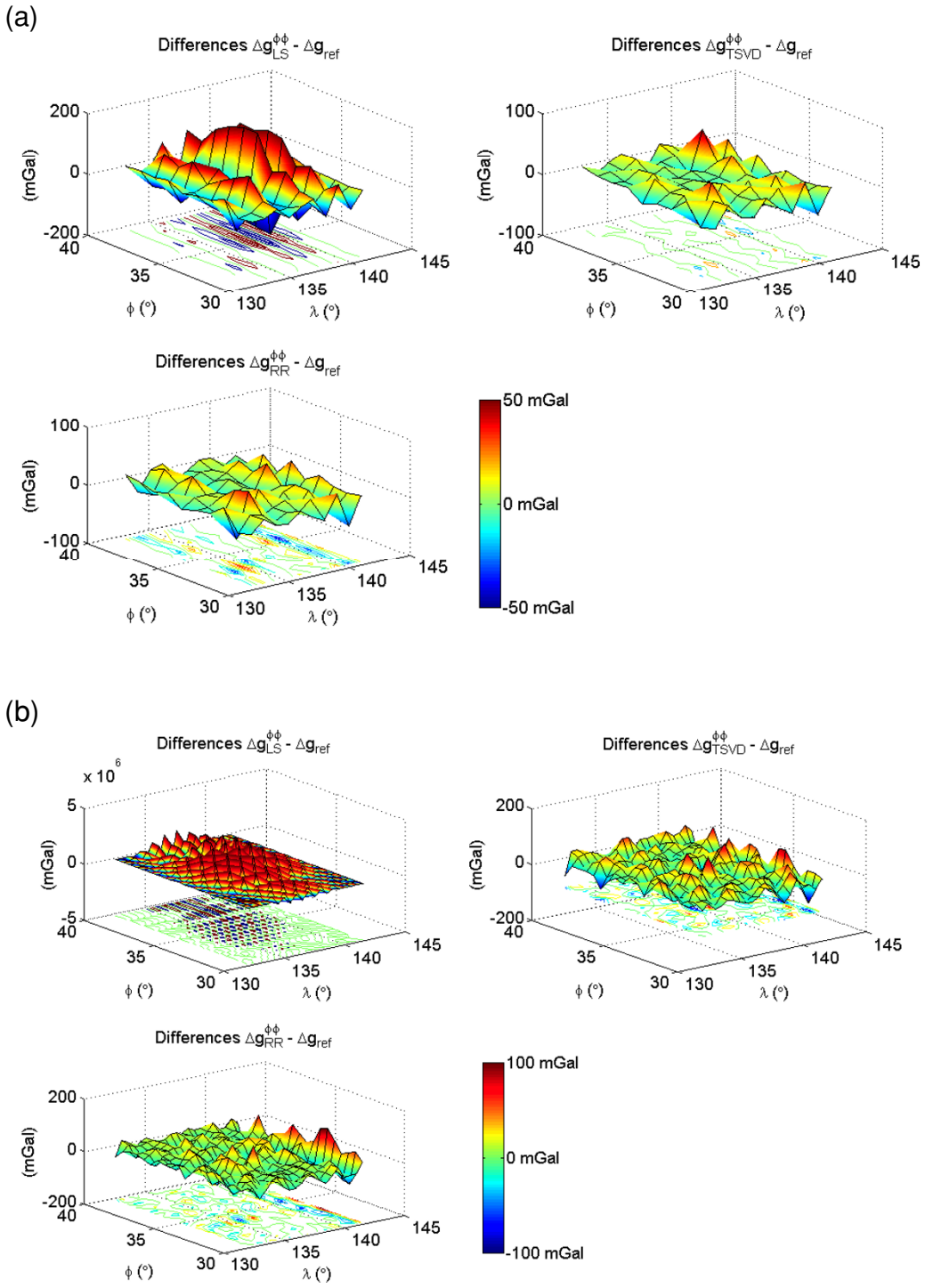

Fig. 3. (a) Example of gravity anomaly differences between the processing results and the true reference in the central part of the region of interest: inverse problem for element $T_{\varphi\varphi}$ (case a). (b) Example of gravity anomaly differences between the processing results and the true reference in the central part of the region of interest: Inverse problem for element $T_{\varphi\varphi}$ (case b).

the particular inverse problems. In both cases (a) and (b), the smallest condition number corresponds to the element $T_{\varphi\lambda}$. Despite this, the RMSE in Tables 1 and 2 for the $T_{\varphi\lambda}$ element is not the best. The biggest condition number in Table 4 corresponds to the element $T_{\varphi\varphi}$. In agreement with this, the RMSE in Tables 1 and 2 for the $T_{\varphi\varphi}$ are the worst.

6. Concluding Remarks

The six inverse problems (Eq. (13)) derived in the first part of the paper are in the form of Fredholm integral equations of the first kind. The inverse of the Fredholm integral equations of the first kind cannot be solved. Therefore, the mathematical properties of these equations easily lead after discretization, see Eq. (14), to numerical instability. The straightforward solutions, such as LS, do not give us sat-

isfactory results, and some kind of regularization method needs to be used. Analyzing the results of our numerical experiments, a number of conclusions can be formulated:

- The best condition number of the normal equations matrix for both cases (a) and (b) has been obtained using the $S_{\varphi\lambda}$ integration kernel; the worst was obtained using the $S_{\varphi\varphi}$ integration kernel.
- The more convenient regularization method seems to be the RR method for both cases (a) and (b).
- The best result, in terms of RMSE, for both cases (a) and (b) has been obtained solving the inverse problem for the T_{rr} component; the worst was obtained for the $T_{\varphi\varphi}$ component.
- The best average RMSE of the output free-air gravity anomaly has been 3.77 mGal using the RR regularization method for case (a) and 13.84 mGal using the RR regularization method for case (b).

In our numerical study, the Gaussian noise was introduced to the observations as the simplest possibility. However, if a realistic stochastic model were assumed, the numerical stability of the system of equations would be changed.

Finally, the question of the optimal combination of the particular solutions to obtain the best gravity anomalies arises. We hope this topic will be the subject of further research.

Acknowledgments. The work presented in this paper started during the Matsumae International Foundation fellowship of the first author at Kyoto University in 2007. The final numerical experiments was supported by the Slovak national project VEGA 1/0775/08 and APVV-0351-07. The work of PX was partly supported by a Grant-in-Aid for Scientific Research B19340129. The authors thank two anonymous reviewers for their valuable comments.

Appendix A. Equation Section 1

Direct and inverse relations between the geocentric Cartesian and spherical coordinate systems:

$$\begin{pmatrix} x \\ y \\ z \end{pmatrix} = \begin{pmatrix} r\cos\varphi\cos\lambda \\ r\cos\varphi\sin\lambda \\ r\sin\varphi \end{pmatrix},$$
$$\begin{pmatrix} r \\ \varphi \\ \lambda \end{pmatrix} = \begin{pmatrix} \sqrt{x^2+y^2+z^2} \\ \arcsin\left(\dfrac{z}{\sqrt{x^2+y^2+z^2}}\right) \\ \arctan\left(\dfrac{y}{x}\right) \end{pmatrix}. \tag{A.1}$$

The Jacobian matrix of transformation between the geocentric Cartesian and spherical coordinate systems (see, for example, Andrilli and Hecker, 2003):

$$\mathbf{J} = \begin{pmatrix} \dfrac{\partial x}{\partial r} & \dfrac{\partial x}{\partial\varphi} & \dfrac{\partial x}{\partial\lambda} \\ \dfrac{\partial y}{\partial r} & \dfrac{\partial y}{\partial\varphi} & \dfrac{\partial y}{\partial\lambda} \\ \dfrac{\partial z}{\partial r} & \dfrac{\partial z}{\partial\varphi} & \dfrac{\partial z}{\partial\lambda} \end{pmatrix} = \begin{pmatrix} \cos\varphi\cos\lambda & r\sin\varphi\cos\lambda & -r\cos\varphi\sin\lambda \\ \cos\varphi\sin\lambda & r\sin\varphi\sin\lambda & r\cos\varphi\cos\lambda \\ \sin\varphi & -r\cos\varphi & 0 \end{pmatrix}. \tag{A.2}$$

The Euclidean distance and the cosine of the spherical distance:

$$\ell = \left(R^2 + r^2 - 2Rr\cos\psi\right)^{1/2}, \tag{A.3}$$
$$\cos\psi = \sin\varphi\sin\varphi' + \cos\varphi\cos\varphi'\cos(\lambda'-\lambda). \tag{A.4}$$

First radial derivatives of the Euclidean distance and of the inverse Euclidean distance:

$$\frac{\partial\ell}{\partial r} = \frac{r - R\cos\psi}{\ell} = \frac{1 - t\cos\psi}{D}, \tag{A.5}$$
$$\frac{\partial}{\partial r}\left(\frac{1}{\ell}\right) = -\frac{r - R\cos\psi}{\ell^3} = -\frac{1 - t\cos\psi}{r^2 D^3}. \tag{A.6}$$

First and second partial derivatives of function $\cos\psi$ according to the φ and λ:

$$\frac{\partial\cos\psi}{\partial\varphi} = \cos\varphi\sin\varphi' - \sin\varphi\cos\varphi'\cos(\lambda'-\lambda) = \sin\psi\cos\alpha = C, \tag{A.7}$$
$$\frac{\partial^2\cos\psi}{\partial\varphi^2} = -\sin\varphi\sin\varphi' - \cos\varphi\cos\varphi'\cos(\lambda'-\lambda) = -\cos\psi, \tag{A.8}$$
$$\frac{\partial\cos\psi}{\partial\lambda} = \cos\varphi\cos\varphi'\sin(\lambda'-\lambda) = \sin\psi\sin\alpha\cos\varphi = E, \tag{A.9}$$
$$\frac{\partial^2\cos\psi}{\partial\lambda^2} = -\cos\varphi\cos\varphi'\cos(\lambda'-\lambda) = \cos\varphi(\sin\psi\sin\varphi\cos\alpha - \cos\psi\cos\varphi) = F, \tag{A.10}$$
$$\frac{\partial^2\cos\psi}{\partial\varphi\partial\lambda} = \frac{\partial^2\cos\psi}{\partial\lambda\partial\varphi} = -\sin\varphi\cos\varphi'\sin(\lambda'-\lambda) = -\sin\psi\sin\alpha\sin\varphi = G. \tag{A.11}$$

Second partial derivatives of generalized Stokes' function $S(t(r,R),\psi(\varphi,\lambda,\varphi',\lambda'))$ according to the geocentric spherical coordinates (r,φ,λ):

$$\begin{aligned}\frac{\partial^2 S(t,\psi)}{\partial\varphi^2} = t^2\Bigg\{&\frac{6tC^2}{D^5} + \frac{3tC^2 - 2\cos\psi}{D^3} - \frac{3\cos\psi}{D} \\ &+ \frac{3t(2C^2 - \cos^2\psi)}{1 - t\cos\psi + D}\left(1 + \frac{1}{D}\right) \\ &+ \frac{3t^2C^2\cos\psi}{D^3(1 - t\cos\psi + D)} \\ &+ \frac{3t^2C^2\cos\psi}{(1 - t\cos\psi + D)^2}\left(1 + \frac{2}{D} + \frac{1}{D^2}\right) \\ &+ \cos\psi\left(5 + 3\ln\frac{1 - t\cos\psi + D}{2}\right)\Bigg\},\end{aligned} \tag{A.12}$$

$$\frac{\partial^2 S(r,\psi)}{\partial\varphi\partial\lambda} = t^2\left\{\frac{6tCE}{D^5}+\frac{3tCE+2G}{D^3}+\frac{3G}{D} +\frac{3t(C^2+CE+G\cos\psi)}{1-t\cos\psi+D}\left(1+\frac{1}{D}\right) +\frac{3t^2CE\cos\psi}{D^3(1-t\cos\psi+D)} +\frac{3t^2CE\cos\psi}{(1-t\cos\psi+D)^2}\left(1+\frac{2}{D}+\frac{1}{D^2}\right) -G\left(5+3\ln\frac{1-t\cos\psi+D}{2}\right)\right\}, \tag{A.13}$$

$$\frac{\partial^2 S(r,\psi)}{\partial\varphi\partial r} = \frac{t^2}{r}\left\{-\frac{6C(1-t\cos\psi)}{D^5}-\frac{C}{D^3}-\frac{6C}{D} -\frac{6tC\cos\psi}{1-t\cos\psi+D}\left(1+\frac{1}{D}\right) +C\left(13+6\ln\frac{1-t\cos\psi+D}{2}\right)\right\}, \tag{A.14}$$

$$\frac{\partial^2 S(r,\psi)}{\partial\lambda^2} = t^2\left\{\frac{6tE^2}{D^5}+\frac{3tE^2+2F}{D^3}+\frac{3F}{D} +\frac{3t(2E^2+F\cos\psi)}{1-t\cos\psi+D}\left(1+\frac{1}{D}\right) +\frac{3t^2E^2\cos\psi}{D^3(1-t\cos\psi+D)} +\frac{3t^2E^2\cos\psi}{(1-t\cos\psi+D)^2}\left(1+\frac{2}{D}+\frac{1}{D^2}\right) -F\left(5+3\ln\frac{1-t\cos\psi+D}{2}\right)\right\}, \tag{A.15}$$

$$\frac{\partial^2 S(r,\psi)}{\partial\lambda\partial r} = \frac{t^2}{r}\left\{-\frac{6E(1-t\cos\psi)}{D^5}-\frac{E}{D^3}-\frac{6E}{D} -\frac{6tE\cos\psi}{1-t\cos\psi+D}\left(1+\frac{1}{D}\right) +E\left(13+6\ln\frac{1-t\cos\psi+D}{2}\right)\right\}, \tag{A.16}$$

$$\frac{\partial^2 S(r,\psi)}{\partial r^2} = \frac{t}{r^2}\left\{(1-t\cos\psi)\left\{\frac{6(1-t\cos\psi)}{D^5}+\frac{3}{D^3}\right\} -\frac{2}{D^3}+\frac{9}{D}-18D+2 -3t\cos\psi\left(15+6\ln\frac{1-t\cos\psi+D}{2}\right)\right\}. \tag{A.17}$$

The particular entries of tensor-valued kernel function **S**:

$$\begin{aligned} S_{\varphi\varphi}(t,\psi,\alpha) &= \frac{1}{r^2}\frac{\partial^2 S(r,\psi,R)}{\partial\varphi^2},\\ S_{\varphi\lambda}(t,\psi,\alpha,\varphi) &= \frac{1}{r^2\cos\varphi}\frac{\partial^2 S(r,\psi,R)}{\partial\varphi\partial\lambda},\\ S_{\varphi r}(t,\psi,\alpha) &= \frac{1}{r}\frac{\partial^2 S(r,\psi,R)}{\partial\varphi\partial r},\\ S_{\lambda\lambda}(t,\psi,\alpha,\varphi) &= \frac{1}{r^2\cos^2\varphi}\frac{\partial^2 S(r,\psi,R)}{\partial\lambda^2},\\ S_{\lambda r}(t,\psi,\alpha,\varphi) &= \frac{1}{r\cos\varphi}\frac{\partial^2 S(r,\psi,R)}{\partial\lambda\partial r},\\ S_{rr}(t,\psi) &= \frac{\partial^2 S(r,\psi,R)}{\partial r^2}. \end{aligned} \tag{A.18}$$

References

Andrilli, S. and D. Hecker, *Elementary Linear Algebra*, 644 pp., Elsevier, Amsterdam, 2003.

Aster, R. C., B. Borchers, and C. H. Thurber, *Parameter Estimation and Inverse Problems*, 301 pp., Elsevier, Amsterdam, 2005.

Bronshtein, I. N., K. A. Semendyayev, G. Musiol, and H. Muehlig, *Handbook of Mathematics*, 1153 pp., Springer, Berlin, 2004.

Drinkwater, M. R., R. Haagmans, D. Muzi, A. Popescu, R. Floberghagen, M. Kern, and M. Fehringer, The GOCE gravity mission: ESA's first core earth explorer, in *Proceedings of the 3rd International GOCE User Workshop*, ESA SP-627, 1–8, 2007.

European Space Agency, *GOCE L1B Products User Handbook*, ESA Technical Note GOCE-GSEG-EOPG-TN-06-0137, 90 s., 2006.

Heiskanen, W. and H. Moritz, *Physical Geodesy*, Freeman, San Francisco, 1967.

Hoerl, A. E. and R. W. Kennard, Ridge regression: biased estimation for nonorthogonal problems, *Technometrics*, **12**, 55–67, 1970.

Kern, M. and R. Haagmans, Determination of gravity gradients from terrestrial gravity data for calibration and validation of gradiometric GOCE data, in *Gravity, Geoid and Space Missions*, edited by Jekeli, Bastos, and Fernandes, 95–100, Springer, Berlin, 2005.

Lemoine, F. G., S. C. Kenyon, J. K. Factor, R. G. Trimmer, N. K. Pavlis, D. S. Chinn, C. M. Cox, S. M. Klosko, S. B. Luthcke, M. H. Torrence, Y. M. Wang, R. G. Williamson, E. C. Pavlis, R. H. Rapp, and T. R. Olson, The development of the joint NASA GSFC and NIMA Geopotential Model EGM96, *NASA Technical Paper NASA/TP-1998-206861*, Goddard Space Flight Center, Greenbelt, USA, 1998.

Martinec, Z., Green's function solution to spherical gradiometric boundary-value problems, *J. Geod.*, **77**, 41–49, 2003.

Novák, P. and E. W. Grafarend, The effect of topographical and atmospheric masses on spaceborne gravimetric and gradiometric data, *Stud. Geophys. Geodaet.*, **50**, 549–582, 2006.

Pizzetti, P., Sopra il calcolo teorico delle deviazioni del geoide dall' ellissoide, *Atti R. Accad. Sci. Torino*, **46**, 331, 1911.

Reed, G. B., Application of kinematical geodesy for determining the short wave length components of the gravity field by satellite gradiometry, *Technical Report No. 201*, Department of Geodetic Science, The Ohio State University, Columbus, Ohio, 1973.

van Gelderen, M. and R. Rummel, The solution of the general geodetic boundary value problem by least squares, *J. Geod.*, **75**, 1–11, 2001.

van Gelderen, M. and R. Rummel, Corrections to "The solution of the general geodetic boundary value problem by least squares", *J. Geod.*, **76**, 121–122, 2002.

Xu, P. L., Determination of surface gravity anomanlies using gradiometric observables, *Geophys. J. Int.*, **110**, 321–332, 1992.

Xu, P. L., Truncated SVD methods for discrete linear ill-posed problems, *Geophys. J. Int.*, **135**, 505–514, 1998.

Xu, P. L. and R. Rummel, Generalized ridge regression with applications in determination of potential fields, *Manuscr. Geod.*, **20**, 8–20, 1994.

J. Janák (e-mail: juraj.janak@stuba.sk), Y. Fukuda, and P. Xu